Springer

Acta Mechanica Sinica

CrossMark click for updates

• RESEARCH PAPER •

Acta Mech. Sin., Vol. 39, 123118 (2023)
https://doi.org/10.1007/s10409-023-23118-x

Laser-induced shock response of shear thickening fluid

Zhoupeng Gu[1,2], Chun Wei[1,3], Xianqian Wu[1,2*], and Chenguang Huang[2,4]

[1] *Key Laboratory of Mechanics in Fluid Solid Coupling Systems, Institute of Mechanics, Chinese Academy of Sciences, Beijing 100190, China;*
[2] *School of Engineering Science, University of Chinese Academy of Sciences, Beijing 100049, China;*
[3] *Institute of Chemical Materials, China Academy of Engineering Physics, Mianyang 621900, China;*
[4] *Hefei Institutes of Physical Science, Chinese Academy of Sciences, Hefei 230031, China*

Received April 14, 2023; accepted May 18, 2023; published online August 25, 2023

It is critical to obtain the shock response of shear thickening fluid (STF) in impact protective engineering. In this paper, we investigated the characteristics of STFs under ultra-high strain rates implemented by laser-induced shock loadings. We fabricated the silica nanoparticle-polyethylene glycol (PEG) STFs with different mass fractions of nanoparticles. The dynamic responses of the water, the PEG, the 40 wt% STF, and the 68 wt% STF with various thicknesses under laser-induced shock loadings were measured. The results showed that the shock wave attenuation increased with the mass fraction of silica nanoparticles, with the highest shock energy dissipation capacity being observed at 68 wt% concentration of STF. According to experimental results, the equations of state (EOS) of the PEG, the 40 wt% STF, and the 68 wt% STF were obtained. This work promoted the understanding of the dynamic behavior of STF and provided a basis for its applications in impact protective engineering.

Shear thickening fluid, Laser-induced shock, Dynamic response, Shock wave attenuation, Equation of state

Citation: Z. Gu, C. Wei, X. Wu, and C. Huang, Laser-induced shock response of shear thickening fluid, Acta Mech. Sin. 39, 123118 (2023), https://doi.org/10.1007/s10409-023-23118-x

1. Introduction

Explosive protection and shock attenuation of materials have attracted significant attention in various applications [1-3]. A variety of materials, including ceramics, porous foam metals, and granular materials, have been discovered to exhibit outstanding explosive protection and shock attenuation capacity at high pressures and strain rates [4-7]. However, the shock wave attenuation characteristics of these materials are generally irreversible, implying that the impact resistances of these materials are lost partly or almost completely after a single impulse loading [8-10], which limits their application in some engineering structures exposed to multiple impulsive loadings [11,12]. Therefore, the demand for intelligent materials with the capacity of reversible shock attenuation and energy absorption is imperative in impact protective engineering.

Intelligent materials such as shear thickening (ST) materials have been extensively studied due to their remarkable capability of reverse response to shock loadings. Upon the cessation of shock loadings, the viscosity of ST materials recovers quickly [13,14]. Shear thickening gel (STG) and shear thickening fluid (STF) are the two main types of ST materials [15-17]. Different from STG, a gel-like state with low crosslinks comprising of boron and siloxane polymers, STF is a non-Newtonian fluid that is composed generally of a high concentration of nanoparticles or microparticles dispersed in a liquid [18,19]. Due to the high impact resistance, both STG and STF have shown remarkable potential for multiple dynamic energy absorption [20,21].

The STFs experience fluid-to-solid transformations under impact loadings, accompanied by a significant increase of viscosity [21,22], which recovers promptly to its initial state after the removal of the external loadings, showing the reversible shock wave attenuation capability [23,24]. In addition, owing to the hard-inorganic nanoparticles with high

*Corresponding author. E-mail address: wuxianqian@imech.ac.cn (Xianqian Wu)
Executive Editor: Xinglong Gong

strength, STFs possess the potential for effective anti-shock loadings [25,26]. Several mechanisms have been proposed to explain the thickening behavior of STF under various loading conditions [16]. Hoffman [27] firstly proposed the order-to-disorder transformation to explain the thickening behavior. However, it is observed experimentally unnecessary. The phenomenon of ST under shear loadings is typically attributed to the hydro-cluster of particles in STFs [28,29], while the dynamic solidification is visible under dynamic compression due to particle jamming phenomena [25,30]. During thickening processes, STF can dissipate tremendous shock energy [23,31], making the STF suitable for a variety of applications in engineering such as armors, dampers, and shock absorbers [32,33].

To better understand the protective behavior of STF at high pressures, it is critical to obtain its dynamic responses including the shock wave propagation and energy absorption. There is a considerable body of knowledge in the literature that addressed the dynamic response of STF under various pressures and loading rates. Waitukaitis and Jaeger [30] performed experiments on maize starch STF under the low-velocity impact of metal rods. The results showed that the STF exhibited solid-like characteristics, which resulted from the jamming transition under compression [34]. Crawford et al. [35] studied the dynamic mechanical behavior of STF synthesized by combining corn starch and water under the impact of falling stones. It was determined that impact-induced thickening occurred in STF with a minimum concentration of 50 wt%; at 52.5 wt%, the STF manifested solid-like properties, causing the rebound of the stone [35,36].

By utilizing a modified split Hopkinson pressure bar (SHPB), the dynamic behavior of STF was investigated, demonstrating its solidification and absorption of a significant amount of energy subjected to impact forces [37,38]. Tan et al. [39] enhanced silica nanoparticle-based STF by incorporating graphene, resulting in a 30% increment in viscosity. The SHPB experiments revealed that the integration of graphene considerably influenced the flow stress of the reinforced STFs, leading to an elevation in peak flow stress [39]. Petel et al. [21,40-42] investigated the responses of various solid particle suspensions amalgamated with ethylene glycol under the high-speed projectile impact (200 m/s to 700 m/s). The corn starch suspensions exhibited no heightened resistance to penetration. For projectile velocities surpassing 500 m/s, the 61 wt% mixture (comprising a 2:1 mass ratio of silica to silicon carbide) offered superior protection compared to the 61% silica suspension, suggesting that the robust particles were more adept at enduring intergranular stress [21,40-42]. Gürgen et al. [43,44] treated fabric composites with STF to improve stab and impact resistance while maintaining flexibility. They also enhanced the impact resistance of cork composite constructions with STF joints [45,46]. Wu et al. [47,48] sealed STF with sandwich panels, and the energy absorption behavior of the STF-filled lattice panels showed significant improvement in specific absorption energy.

However, the aforementioned studies on the impact resistance of STF are limited to low pressure conditions [49]. In view of this, Wu et al. [31,50] firstly studied the dynamic response of 57% (vol/vol) STF under laser-induced shock loadings with peak pressures of several GPa, revealing a rapid attenuation of shock waves and excellent energy absorption capacity. However, the effects of the mass fraction of nanoparticles on the shock response of STF are still unknown.

In this study, we investigated the shock responses of the water, the polyethylene glycol (PEG), the 40 wt% STF, and the 68 wt% STF subjected to laser-induced shock. We measured the equations of state (EOS) of these materials and obtained their shock wave attenuation behavior. The effects of the mass fraction of nanoparticles were also investigated. The paper is organized as follows. Section 2 provides an overview of the methods for preparing materials and for evaluating their shock wave attenuation. In Sect. 3, the shock dissipation capacities of STFs are analyzed, and the equations of state are obtained, followed by related discussion and conclusions.

2. Materials and methods

This section delineates the fabrication of materials and the laser-induced shock experiments. The STFs with different mass fractions were sandwiched with various thicknesses between two metal sheets. A photonic Doppler velocimetry (PDV) system was used to measure the free-surface velocity of one metal sheet, which was used to determine the dynamic responses of the materials. The thin layers of the water and the PEG were also measured as a comparison.

2.1 Materials preparation

The enhanced Stöber method [51] was used to grow colloidal nanoparticles, as depicted in Fig. 1a. Anhydrous ethanol and ammonia were combined uniformly in a reactor, and a tetraethyl orthosilicate ethanol dispersion was added at a specific rate using a peristaltic pump while mechanical agitation was carried out at 40 °C for 2 h, followed by a 24-hour reaction period. Most of the solvent was then evaporated at 60 °C to obtain a concentrated suspension with a silica nanoparticle mass fraction of 10%-15%. The concentrated suspension was subsequently mixed with PEG-200 via mechanical stirring to obtain silica-PEG STFs with various mass fractions. The ethanol was removed via rotary evaporation at 60 °C. The scanning electron microscope

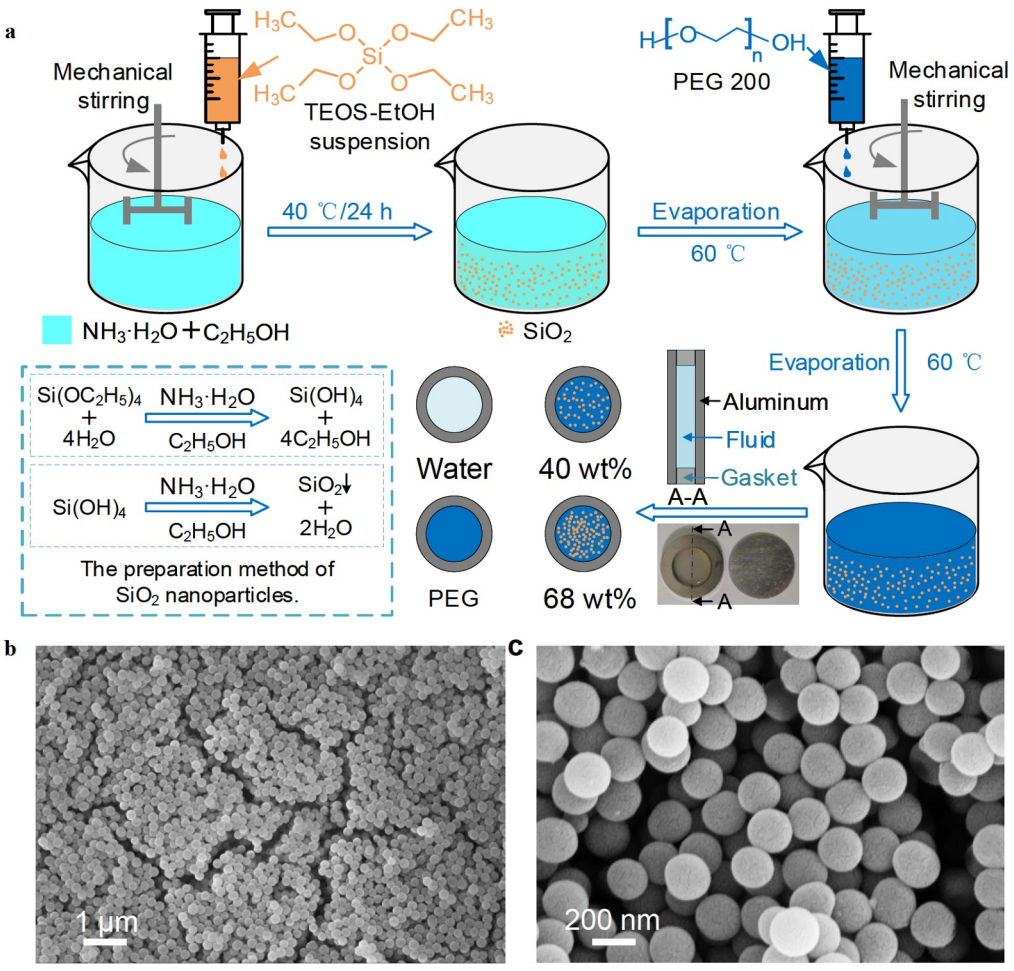

Figure 1 **a** Method of preparing silica nanoparticles and samples [51,52]. **b**, **c** SEM images of the silica nanoparticles.

(SEM) was used to analyze the morphology of the silica nanoparticles, as shown in Fig. 1b and c. The monodisperse spherical silica nanoparticles had an average size of approximately 210 nm. Two Φ25.4×0.5 mm aluminum plates sandwiched a gasket with different thicknesses to form a mold for preparing samples. The gaskets had an outer diameter of 25.4 mm and an inner diameter of 15.0 mm, and its thickness varied from 0.1 to 2.0 mm to fabricate the samples with different thicknesses.

In order to understand the shock loading behavior of STF with a relatively wide range of nanoparticle mass fractions, the 40 wt% and 68 wt% STF, which are widely used in engineering, were studied. As a reference, the water and the PEG were also investigated. The densities of the water, the PEG, the 40 wt% STF, and the 68 wt% STF were 1.000 g/cm^3, 1.125 g/cm^3, 1.330 g/cm^3, and 1.540 g/cm^3, respectively.

The rheology of the materials were measured using a Kinexus Pro+ rotating rheometer with a 40 mm 4° cone and plate equipped with temperature control set to 25 °C [50]. The steady-state shear viscosity and shear stress of the PEG, the 40 wt% STF, and the 68 wt% STF at different shear strain rates were measured, as shown in Fig. 2a and b. With increasing the mass fraction of silica nanoparticles from 0 to 40%, the viscosity of the material increases from 0.052 to 0.134 Pa·s, respectively, at the shear rate of 0.2 s^{-1}, and shear stress increases linearly with increasing the shear rate, showing the behavior of Newtonian fluids. However, the 68 wt% STF with an initial viscosity of 24 Pa·s exhibits shear-thinning behavior at low shear rates, followed by a sudden increase in viscosity at a critical shear strain rate of approximately 24 s^{-1}, indicating the onset of ST.

2.2 Experimental method

Figure 3a and b shows the configuration of the laser-induced shock experiments [50]. A 30-μm-thick thin aluminum film glued firmly on a 4-mm-thick BK7 glass is vaporized and ionized under the irradiation of a high-power density laser (Q-switched Nd: YAG laser, wavelength ~1064 nm, maximum output energy ~2.5 J, and FWHM ~10 ns), generating a shock pressure with a high amplitude of several GPa and a short duration of tens of nanoseconds as shown in Fig. 3c [53-56]. The shock pressure reaches a peak of about 7 GPa

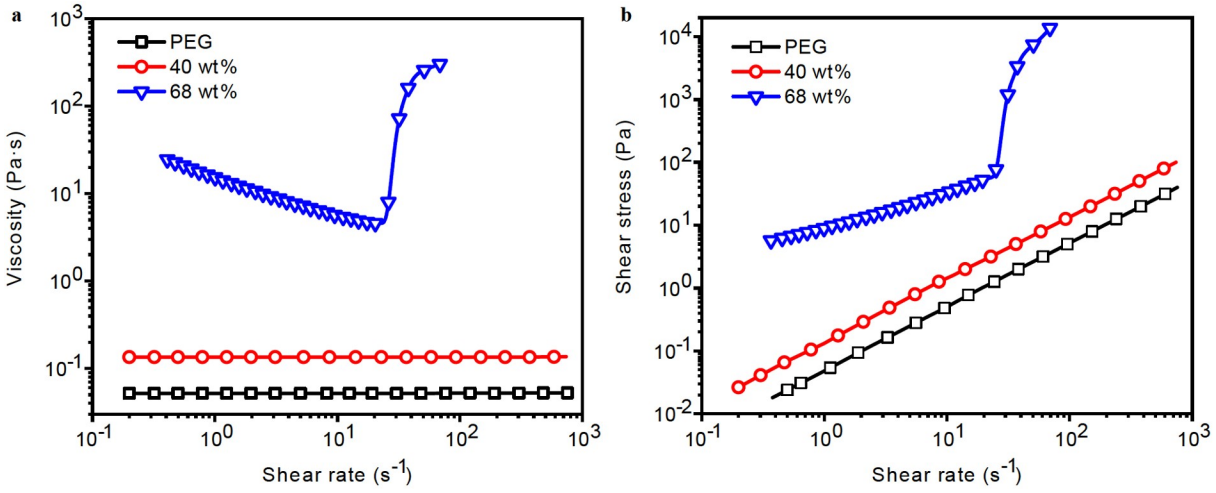

Figure 2 **a** Steady-state shear viscosities and **b** shear stress of the PEG, the 40 wt% STF, and the 68 wt% STF at various shear rates.

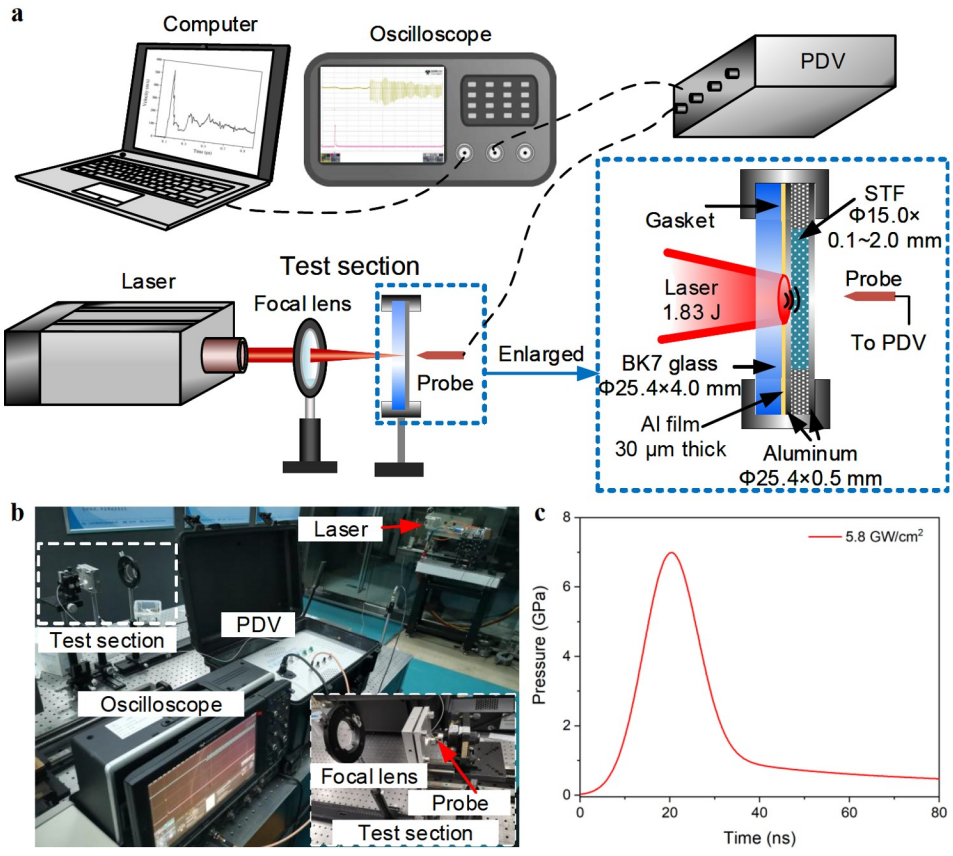

Figure 3 **a** Schematic and **b** configuration of the laser-induced shock experiments. A high-intensity laser beam generates plasma with a pressure of several GPa on the surface of an aluminum plate [53]. **c** Shock pressure profiles at 5.8 GW/cm^3 analyzed by the coupling model [54,55].

during laser irradiation with a maximum power density of 5.8 GW/cm^2, followed by a gradual decrease due to plasma cooling after the laser is switched off. The shock wave propagates through the sample material, resulting in a rapid velocity of the free-surface of the sample. The free-surface velocities of the assembled samples are measured using PDV, based on the configuration of Strand et al. [57], as depicted in Fig. 4a. The PDV system consists of an optical collimating lens probe, a high-power 1550 nm continuous wave (CW) distributed feedback laser, a photodiode detector, and a fiber optic circulator [58]. The probe emits the reference light with a frequency f_0 and collects the Doppler-shifted light with a frequency f_b reflected from the moving surface of the target. The velocity of the measured surface of

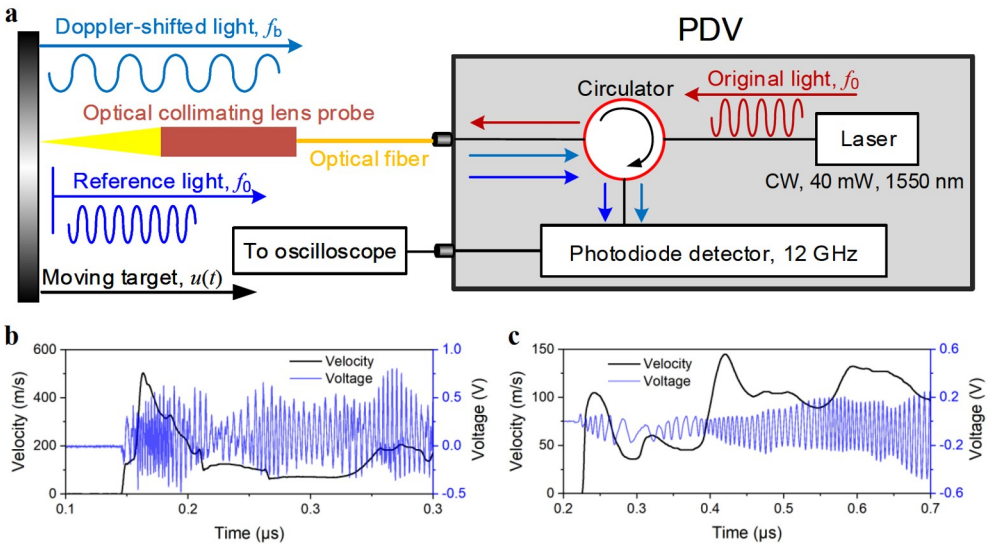

Figure 4 **a** PDV system configuration [58] and the measured interference fringes and free-surface velocities of **b** a single aluminum plate and **c** two aluminum plates sandwiched the 0.1-mm-thick water sample under laser-induced shock.

the moving target, $v(t)$, is calculated according to the difference between f_0 and f_b,

$$v(t) = \frac{\lambda_0}{2} f(t) \tag{1}$$

where λ_0 is the initial operating wavelength of the CW laser, $f(t) = f_0 - f_b(t)$.

Figure 4b and c shows the typical interference fringes and the corresponding velocity history for a single aluminum plate and two aluminum plates sandwiched a 0.1-mm-thick water sample, respectively. The closer the adjacent interference fringes are, the faster the velocity is.

Figure 5 shows the measured and simulated back free-surface velocities of the single aluminum plate. Details of the numerical simulations will be presented later. The two measurements peak velocities are 506.6 m/s and 512.8 m/s, a difference by 1.2%, indicating the high repeatability of the experiments. When the shock wave arrives at the back free-surface, the particle velocity increases abruptly. At 114 ns, it attains the peak value, followed by a quick drop to 78 m/s at 251 ns. The shock wave reflects between the loading surface and the back free-surface of the aluminum plate, resulting in several distinct peaks and valleys. The intervals between the peaks increase due to the decrease of the shock wave speed resulting from the energy dissipation in the aluminum plate [31]. The back free-surface velocity fluctuation disappears gradually after 592 ns when the stress wave reaches almost equilibrium.

Figure 6 depicts schematically the propagation of the shock wave with the peak pressure, P_m, in the aluminum-STF-aluminum sandwiched structure. The shock wave propagates in the left-side aluminum plate and reaches the interface (point 2) between the aluminum plate and the STF. Due to the differences in wave impedances, a portion of the wave is transmitted into the STF while the rest is reflected

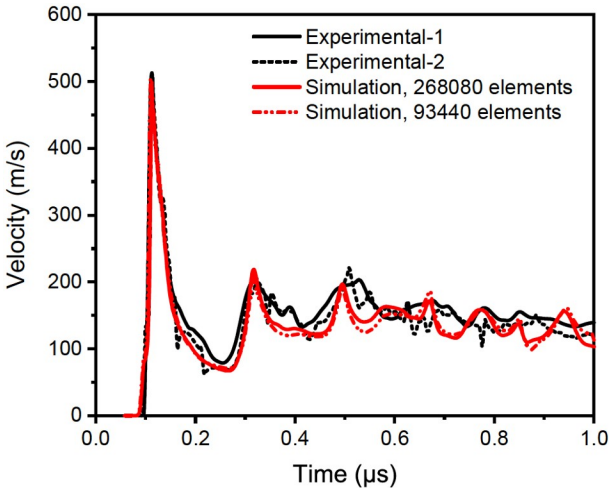

Figure 5 Back free-surface velocity of the aluminum plate obtained by laser-induced shock experiments and numerical simulations.

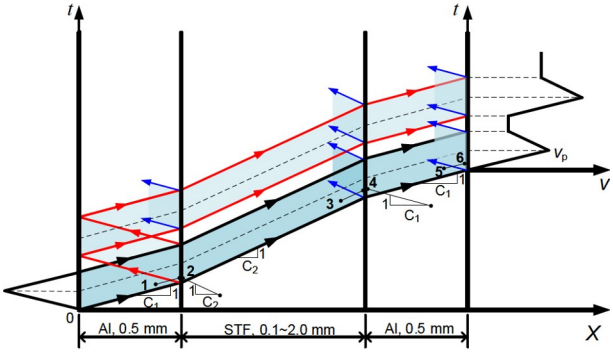

Figure 6 Characteristic analysis of the shock wave in the aluminum-STF-aluminum sandwich structure. The first peak of the back free-surface velocity is used to analyze the shock wave attenuation behavior of the STF.

into the aluminum plate. The shock wave travels in the STF until it reaches the interface (point 4) on the right side of the sample, where another portion of the shock wave is transmitted into the aluminum plate. The loading wave continues to propagate through the right-side aluminum plate, resulting in the initial peak velocity, V_p, at the free-surface (point 6). Multiple reflections of the shock wave lead to several peaks of the particle velocity. In this study, we evaluate the shock wave attenuation of the STFs based on the first peak velocity.

After the initial peak velocities at the back free-surface (v_6 at point 6) of samples with various thicknesses were measured, numerical simulations were then performed to obtain the peak velocities at point 4 (v_4). Consequently, the peak velocity at point 3 can be determined as

$$v_3 = \frac{\rho_{\mathrm{Al}} c_{\mathrm{Al}} + \rho_{\mathrm{STF}} c_{\mathrm{STF}}}{2\rho_{\mathrm{STF}} c_{\mathrm{STF}}} v_4, \tag{2}$$

where ρ_{Al} and c_{Al} represent the density and shock wave speed of the aluminum plate, while ρ_{STF} and c_{STF} refer to the density and shock wave speed of the STF. The peak stress of the STF at point 3 can be expressed as

$$\sigma_3 = \rho_{\mathrm{STF}} C_{\mathrm{STF}} v_3. \tag{3}$$

To analyze the attenuation behavior of the shock wave in the STFs, we changed the thickness of the STF to obtain the different velocities and stresses at point 3 [31].

2.3 Numerical simulation model

To determine the velocity, v_4, a numerical simulation model, as shown in Fig. 7, was established using LS-DYNA software [59,60] to obtain the shock wave attenuation of the aluminum plate. A 1/4 model was built to enhance the computational efficiency due to the symmetry of the model. The aluminum plate had a radius of 15 mm and a thickness of 0.5 mm, with symmetrical boundary constraints using the *BOUNDARY_SPC_SE keyword. The shock wave pressure was applied on the upper surface of the plate through the *LOAD_SEGMENT_SET keyword [53]. The model was fine-meshed with 268080 hexahedral Lagrangian elements, and the minimum element length was 0.01 mm in the loading area to ensure adequate numerical accuracy.

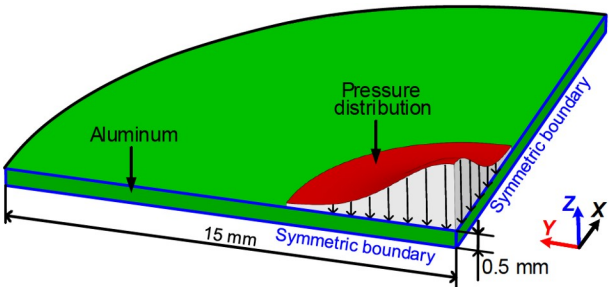

Figure 7 Schematic diagram of the numerical simulation model of the aluminum plate under shock loading.

The tempo-spatial distribution of the shock pressure is expressed as

$$p(t,r) = p(t)\mathrm{e}^{-2\frac{r^2}{R^2}}, \tag{4}$$

where $p(t)$ notes the temporal distribution of the shock wave, r denotes the distance from the laser beam center, and R is the laser radius [54,55].

The temporal distribution of the shock pressure, $p(t)$, for a maximum laser power density of 5.8 GW/cm^2 is shown in Fig. 3c. The Johnson-Cook constitutive model *MAT_JOHNSON_COOK [55,61] was used to describe the dynamic behavior of the 2024 aluminum plate under shock loadings. The effective stress is determined as

$$\sigma_y = \left(A + B\overline{\varepsilon^P}^n\right)\left(1 + C\ln\dot{\varepsilon}^*\right)\left[1 - \left(\frac{T - T_{\mathrm{room}}}{T_{\mathrm{melt}} - T_{\mathrm{room}}}\right)^m\right], \tag{5}$$

where A, B, and C denote material parameters, $\overline{\varepsilon^P}$ indicates equivalent plastic strain, n presents strain-hardening exponent, $\dot{\varepsilon}^*$ notes normalized equivalent plastic strain rate, T_{room} is initial temperature, T_{melt} is melting temperature, and m represents the thermal softening constant [47]. The Mie-Grüneisen equation of state (EOS) *EOS_GRUNEISEN was used to describe the compressibility of the 2024 aluminum plate, and the pressure is expressed as

$$P = \frac{\rho_0 c_0^2 \mu_0 \left[1 + \left(1 - \frac{\kappa_0}{2}\mu_0\right) - \frac{a}{2}\mu_0^2\right]}{\left[1 - (s_1 - 1)\mu_0 - s_2\frac{\mu_0^2}{\mu_0 + 1} - s_3\frac{\mu_0^8}{(\mu_0 + 1)^2}\right]^2} + (\kappa_0 + a\mu_0)E_0, \tag{6}$$

where $\mu_0 = \rho/\rho_0 - 1$, c_0 is the intercept of the shock wave velocity and particle velocity curve, s_1, s_2, and s_3 are fitted parameters, ρ_0 is initial density, ρ is present density, and E_0 is initial internal energy [62,63]. The parameters of the numerical simulation are listed in Tables 1 and 2.

The mesh sensitivity analysis of the aluminum plate subjected to the shock loading is conducted as shown in Fig. 5. The maximum peak velocities for the simulations with 268080 and 93440 elements are 502.7 m/s and 498.5 m/s, respectively, indicating the convergency of the model. In addition, the peak velocity for the simulation with 268080 elements is almost identical to the experimental results, validating the numerical simulation model. Figure 8a and b shows the particle velocity profiles at different depths and the decay of the peak particle velocities along depths of a single infinitely-thick aluminum plate. As shown in Fig. 8a, at the shock surface the particle velocity increases rapidly to the peak value of 433.5 m/s, and the elastic and plastic waves propagate in the plate. The elastic wave-front precedes the plastic wave-front with the increasing depth due to

Table 1 Johnson-Cook material properties of the aluminum plate [53]

E_0 (GPa)	v	A (MPa)	B (MPa)	C	n	T_{room} (K)	T_{melt} (K)	m
72	0.34	200	426	0.0615	0.34	294	893	0.895

Table 2 Mie-Grüneisen EOS parameters of the aluminum plate [53]

ρ (kg·m^{-3})	C_0 (m·s^{-1})	S_1	S_2	S_3	κ_0	a
2700	5164	1.31	0	0	2	0.46

faster elastic wave speed [56]. The peak velocity drops to 252.8 m/s at the depth of 0.5 mm and to 143.0 m/s at the depth of 1.0 mm. After that, the shock wave experiences less attenuation with the increasing depth due to the decrease of local strain rate, plastic strain, and plastic stress [53,54]. Only the elastic wave propagates in the aluminum plate for depths greater than 3.0 mm, resulting in negligible attenuation. The attenuation of the peak particle velocity obeys approximately an exponential function:

$$V_{\mathrm{p}} = \beta_0 \mathrm{e}^{-\frac{h}{\alpha_0}} + \gamma_0, \tag{7}$$

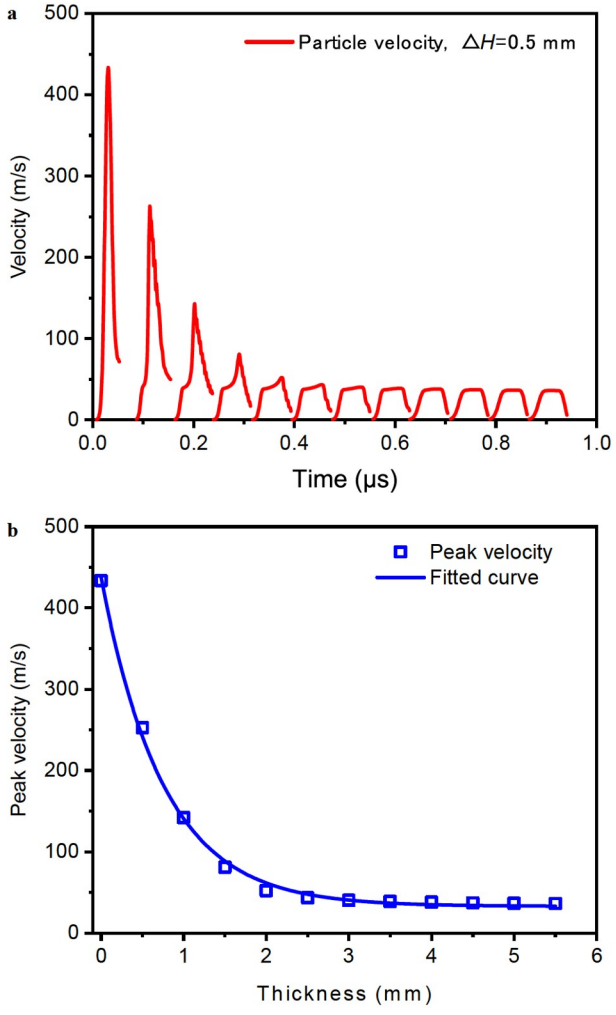

Figure 8 **a** Particle velocity profiles at different depths and **b** decay of the peak particle velocities in depths in an infinitely-thick aluminum plate under shock wave.

where h is the depth of the aluminum plate, and V_{p} is the peak particle velocity [56]. Equation (7) can address the decay capacity of the material subjected to a shock loading. When h equals zero, the expression $V_{\mathrm{p}} = \beta_0 + \gamma_0$ represents the velocity at the initial position. The variable α_0 denotes the decay index of the shock loading. According to Eq. (7), a smaller value of α_0 and a larger value of β_0 will result in quick attenuation of V_{p}. Subsequently, the capacity for shock wave attenuation of the STF can be assessed based on the parameters α_0 and β_0.

The fitted curve, as shown in Fig. 8b, can be expressed as

$$V_{\text{6-Al}} = 404.7\mathrm{e}^{-\frac{h}{0.775}} + 32.9, \tag{8}$$

where h is in mm and $V_{\text{6-Al}}$ is in m/s.

3. Results and discussion

This section measured the back free-surface velocities (at point 6 in Fig. 6) of several materials under laser-induced shock loading, from which the attenuations of peak velocities at the fluid-aluminum plate interface, v_4, were deduced. The EOS of the STFs was derived to determine the pressure attenuation.

3.1 Experimental results

Figure 9 shows the back free-surface velocities (at point 6 in Fig. 6) of the water, the PEG, the 40 wt% STF, and the 68 wt % STF with various thicknesses under laser-induced shock. Each thickness was tested with two samples. The peak velocities and the arrival times of the two tests showed errors within 3% and 1.0%, respectively. To diminish the errors, the average peak velocity and the average peak velocity arrival time of the two repeated tests were utilized. For the same thickness, the water has the lowest back free-surface peak velocity, v_6, due to the impedance mismatch effect. While back free-surface peak velocity increases with increasing the mass fraction of the silica nanoparticles. The 68 wt% STF shows the highest peak velocity, v_6, followed by the 40 wt% STF, the PEG, and the water.

Figure 10a shows the back free-surface peak velocity, v_6, and the fitting curves for the water, the PEG, the 40 wt% STF, and the 68 wt% STF with various thicknesses. The

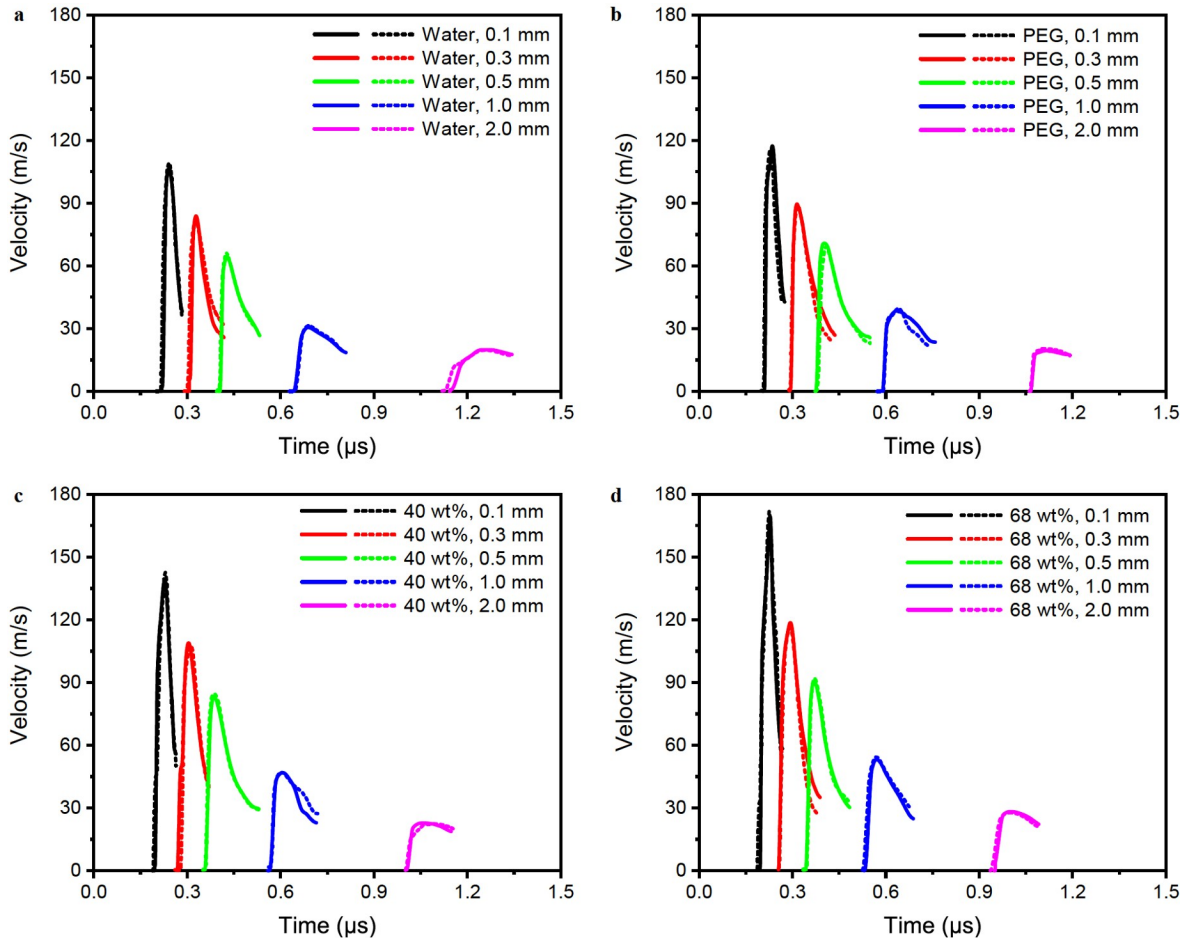

Figure 9 Free-surface velocities (at point 6 in Fig. 6) of **a** the water, **b** the PEG, **c** the 40 wt% STF, and **d** the 68 wt% STF with various thicknesses.

attenuation of v_6 along the thickness can be fitted by Eq. (8):

$$V_{\text{6-water}} = 112.8\text{e}^{-\frac{h}{0.609}} + 13.4, \tag{9}$$

$$V_{\text{6-PEG}} = 119.3\text{e}^{-\frac{h}{0.639}} + 15.1, \tag{10}$$

$$V_{\text{6-40STF}} = 147.1\text{e}^{-\frac{h}{0.685}} + 14.2, \tag{11}$$

$$V_{\text{6-68STF}} = 177.8\text{e}^{-\frac{h}{0.559}} + 23.2, \tag{12}$$

where $V_{\text{6-water}}$, $V_{\text{6-PEG}}$, $V_{\text{6-40STF}}$, and $V_{\text{6-68STF}}$ represent back free-surface peak velocities of the water, the PEG, the 40 wt% STF, and the 68 wt% STF, respectively with a unit of m/s; while h denotes sample thickness in mm. The fitted formulas revealed that the 68 wt% STF has the smallest α_0 and the largest β_0, indicating the fastest attenuation of the shock wave in the 68 wt% STF. From 0.1 to 2.0 mm in thickness, the v_6 of the water, the PEG, the 40 wt% STF, and the 68 wt% STF dropped by 88.0 m/s, 92.2 m/s, 119.2 m/s, and 143.7 m/s, respectively. The decrease in the v_6 of the 68 wt% STF was 1.63, 1.56, and 1.21 times that of the water, the PEG, and the 40 wt% STF, respectively.

Assuming the shock wave takes the same time to go through the right-side aluminum plate, the difference in the arrival time of the v_6 of materials with various thicknesses could be utilized to determine the shock wave speed of the fluids. The shock wave velocities and the fitting curves of the water, the PEG, the 40 wt% STF, and the 68 wt% STF at different positions are shown in Fig. 10b, which can be written as

$$U_{\text{S-water}} = 827\text{e}^{-\frac{h}{0.461}} + 1761, \tag{13}$$

$$U_{\text{S-PEG}} = 517\text{e}^{-\frac{h}{0.387}} + 2078, \tag{14}$$

$$U_{\text{S-40STF}} = 733\text{e}^{-\frac{h}{0.429}} + 2179, \tag{15}$$

$$U_{\text{S-68STF}} = 873\text{e}^{-\frac{h}{0.448}} + 2314, \tag{16}$$

where $U_{\text{S-water}}$, $U_{\text{S-PEG}}$, $U_{\text{S-40STF}}$, and $U_{\text{S-68STF}}$ are shock wave velocities of the water, the PEG, the 40 wt% STF, and the 68 wt% STF, respectively, with a unit of m/s; and h is the position along the thickness of the sample with a unit of mm. The shock wave velocity decreases as the thickness of the sample increases. The 68 wt% STF has the highest shock wave velocity, followed by the 40 wt% STF, the PEG, and the water.

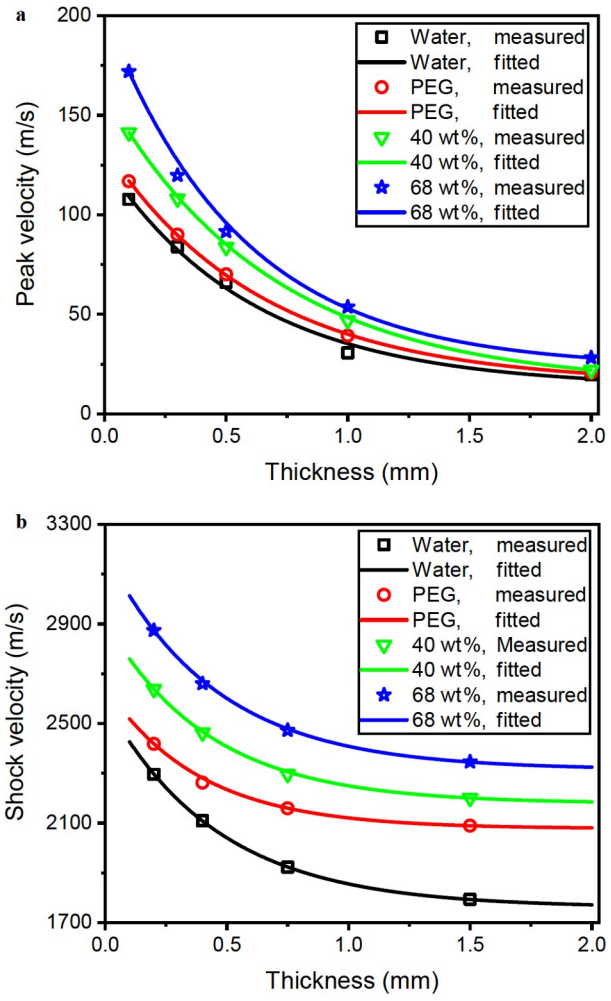

Figure 10 **a** Back free-surface peak velocities, v_6, and **b** shock wave velocities of the water, the PEG, the 40 wt% STF, and the 68 wt% STF at various positions.

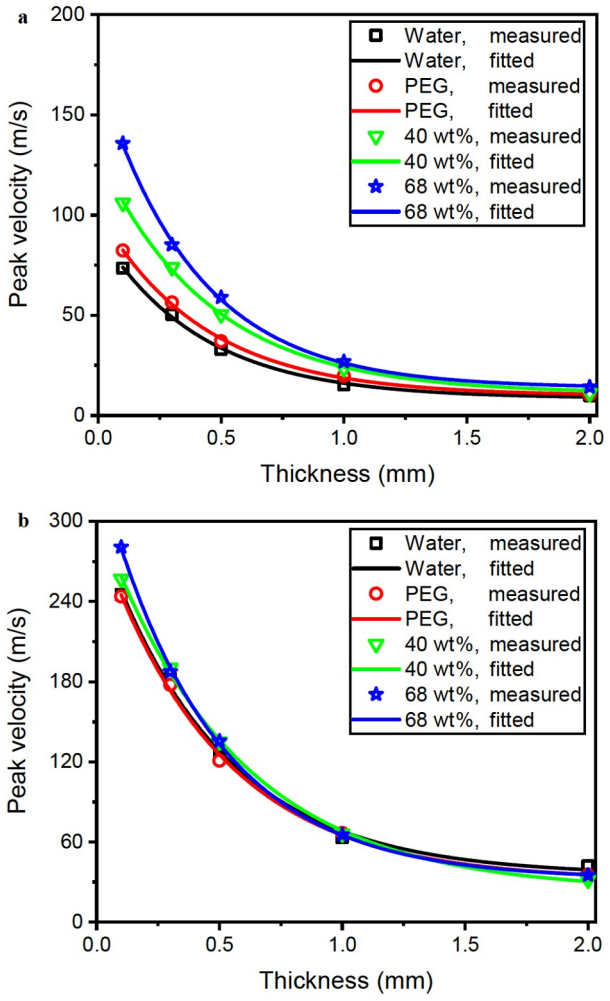

Figure 11 **a** Interface peak velocities, v_4, and **b** peak velocities at point 3, v_3, as depicted in Fig. 6, of the water, the PEG, the 40 wt% STF, and the 68 wt% STF with various thicknesses.

3.2 Equation of state

Figure 11a shows the calculated interface peak velocity, v_4, at point 4 as depicted in Fig. 6 and the fitting curves for the water, the PEG, the 40 wt% STF, and the 68 wt% STF at different positions according to Fig. 8 and Eq. (8). The attenuation behaviors of v_4 are fitted as

$$V_{4-\text{water}} = 83.1\text{e}^{-\frac{h}{0.417}} + 8.5, \tag{17}$$

$$V_{4\text{-PEG}} = 91.8\text{e}^{-\frac{h}{0.428}} + 9.8, \tag{18}$$

$$V_{4\text{-40STF}} = 119.3\text{e}^{-\frac{h}{0.453}} + 11.0, \tag{19}$$

$$V_{4\text{-68STF}} = 156.4\text{e}^{-\frac{h}{0.395}} + 13.7, \tag{20}$$

where $V_{4\text{-water}}$, $V_{4\text{-PEG}}$, $V_{4\text{-40STF}}$, and $V_{4\text{-68STF}}$ are v_4 of the water, the PEG, the 40 wt% STF, and the 68 wt% STF, respectively, with a unit of m/s; and h is the thickness of the sample with a unit of mm. The 68 wt% STF shows the fastest attenuation of the v_4 due to the smallest α_0 and the largest β_0 compared to the water, the PEG, and the 40 wt% STF. The v_4 of the water, the PEG, the 40 wt% STF, and the 68 wt% STF decrease by 68.6%, 87.5%, 89.2%, and 89.6%, respectively, as the sample thickness increases from 0.1 to 2 mm.

To determine the EOS of the STFs, we need to calculate the peak particle velocity, v_3, at point 3 as depicted in Fig. 6 by Eq. (2). Figure 11b shows the v_3 of the water, the PEG, the 40 wt% STF, and the 68 wt% STF, which can be described as

$$V_{3\text{-water}} = 261.9\text{e}^{-\frac{h}{0.482}} + 35.1, \tag{21}$$

$$V_{3\text{-PEG}} = 262.3\text{e}^{-\frac{h}{0.488}} + 31.2, \tag{22}$$

$$V_{3\text{-40STF}} = 282.8\text{e}^{-\frac{h}{0.546}} + 23.2, \tag{23}$$

$$V_{3\text{-68STF}} = 309.8\text{e}^{-\frac{h}{0.447}} + 31.9, \tag{24}$$

where $V_{3-\text{water}}$, $V_{3-\text{PEG}}$, $V_{3-40\text{STF}}$, and $V_{3-68\text{STF}}$ are v_3 of the water, the PEG, the 40 wt% STF, and the 68 wt% STF, respectively, with a unit of m/s; and h is the position along the thickness of the sample with a unit of mm. From 0.1 to 2.0 mm, the v_3 of the water, the PEG, the 40 wt% STF, and the 68 wt% STF dropped by 203.3 m/s, 207.8 m/s, 225.3 m/s, and 245.6 m/s, respectively.

The Mie-Grüneisen EOS, which describes the bulk compressibility of materials, is crucial for understanding the shock loading behavior of materials. It provides the fundamental data for modeling the behavior of materials subjected to explosive and impact loadings, enabling the design and optimization of materials with high-impact resistance. The first-order and the second-order Mie-Grüneisen EOS are expressed as

$$U_S = C_0 + S_1 U_P, \tag{25}$$

$$U_S = C_0 + S_1 U_P + S_2 U_P^2, \tag{26}$$

where U_S and U_P are shock wave velocity and particle velocity, respectively, with unit of km/s; C_0, S_1, and S_2 are fitted parameters according to U_S and U_P [64]. The first-order Mie-Grüneisen EOS has a linear relationship between the particle velocity and the shock wave velocity, which is commonly used for solid materials [65]. The second-order Mie-Grüneisen EOS is generally suitable for a wide range of materials especially liquids and polymers [66].

Figure 12a shows the relationships between the particle velocity and the shock wave velocity for the water, the PEG, the 40 wt% STF, and the 68 wt% STF. Both the first-order and the second-order Mie-Grüneisen EOS are employed to fit the curves. The second-order Mie-Grüneisen EOS curve for water in Ref. [62] is also included. The Mie-Grüneisen EOS for the water, obtained from both the present experiments and the literature, can be expressed as

$$U_{\text{S-water-1st}} = 1.64 + 3.12 U_P, \tag{27}$$

$$U_{\text{S-water-2nd}} = 1.67 + 2.63 U_P + 1.77 U_P^2, \tag{28}$$

$$U_{\text{S-water-Ref}} = 1.65 + 2.56 U_P + 1.93 U_P^2, \tag{29}$$

where $U_{\text{S-water-1st}}$ and $U_{\text{S-water-2nd}}$ denote the shock wave velocity of the first-order and the second-order Mie-Grüneisen EOS of the water, respectively; while $U_{\text{S-water-Ref}}$ represents the shock wave velocity of Mie-Grüneisen EOS of the water in Ref. [62]. The parameters of the fitted Mie-Grüneisen EOS are close to the values given by Ref. [62], validating the experimental measurements. Both the first-order and the second-order Mie-Grüneisen EOS could be used to describe bulk compressibility of the water within the range of experimental particle velocities below 280 m/s, as shown in Fig. 12a. However, for particle velocities above 280 m/s, the first-order Mie-Grüneisen EOS for the water deviates from the EOS curve in Ref. [62], while the second-order Mie-Grüneisen EOS agrees well with Ref. [62].

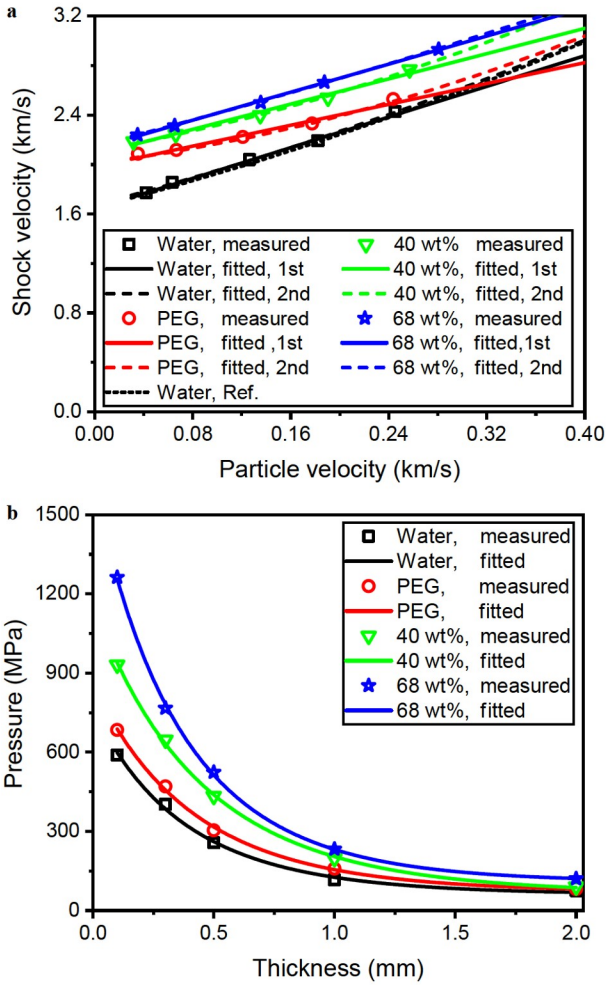

Figure 12 **a** Relationships between the particle velocity and shock wave velocity. **b** Attenuation of peak shock pressure for the water, the PEG, the 40 wt% STF, and the 68 wt% STF.

The first-order Mie-Grüneisen EOS for the PEG, the 40 wt% STF, and the 68 wt% STF are given as

$$U_{\text{S-PEG-1st}} = 1.98 + 2.11 U_P, \tag{30}$$

$$U_{\text{S-40STF-1st}} = 2.08 + 2.55 U_P, \tag{31}$$

$$U_{\text{S-68STF-1st}} = 2.13 + 2.84 U_P, \tag{32}$$

where $U_{\text{S-PEG-1st}}$, $U_{\text{S-40STF-1st}}$, and $U_{\text{S-68STF-1st}}$ represent shock wave velocities of the first-order Mie-Grüneisen EOS of the PEG, the 40 wt% STF, and the 68 wt% STF, respectively. The second-order Mie-Grüneisen EOS for the PEG, the 40 wt% STF, and the 68 wt% STF are given as

$$U_{\text{S-PEG-2nd}} = 2.02 + 1.24 U_P + 3.36 U_P^2, \tag{33}$$

$$U_{\text{S-40STF-2nd}} = 2.11 + 1.73 U_P + 3.17 U_P^2, \tag{34}$$

$$U_{\text{S-68STF-2nd}} = 2.15 + 2.54 U_P + 0.94 U_P^2, \tag{35}$$

where $U_{\text{S-PEG-2nd}}$, $U_{\text{S-40STF-2nd}}$, and $U_{\text{S-68STF-2nd}}$ denote shock wave velocities of the second-order Mie-Grüneisen EOS of

the PEG, the 40 wt% STF, and the 68 wt% STF, respectively.

As shown in Fig. 12a, in the particle velocity range of the laser-induced shock test, the first-order and the second-order Mie-Grüneisen EOS do not exhibit obvious differences. The first-order and second-order Mie-Grüneisen EOS give almost the same C_1 values for the same material. The C_1 of the STFs increases with increasing the mass fraction of silica nanoparticles, indicating the higher shock wave velocity at zero pressure for the larger mass fraction of silica nanoparticles. The increase of the mass fraction of silica nanoparticles also leads to an increase of S_1 of the first-order Mie-Grüneisen EOS, indicating the faster increase of shock wave velocity with respect to the particle velocity for the 68 wt% STF compared to the 40 wt% STF. Similarly, the S_1 of the second-order Mie-Grüneisen EOS also increases with increasing mass fraction of silica nanoparticles. However, the S_1 of the second-order EOS is smaller than that of the first-order EOS, and the difference decreases with the increasing mass fraction of silica nanoparticles. As the mass fraction of silica nanoparticles increases, the S_2 of the second-order EOS decreases. Consequently, at high particle velocities, the deviation between the first-order and the second-order Mie-Grüneisen EOS decreases with increasing mass fraction of silica. For the 68 wt% STF, the first-order and the second-order EOS are almost identical, which might be ascribed to the thickening behavior of 68 wt% STF under shock that makes it behave like a solid material. However, for the other materials, the first-order and the second-order EOS deviate obviously at high particle velocity, implying that they still behave as fluids under laser-induced shock. Due to the limitation of our laser-induced shock conditions, experiments with higher shock velocities were not performed. Future studies will be investigated to understand the shock behavior of STFs at even higher shock pressures.

Once the EOS of the materials is obtained, the shock pressure at point 3, as depicted in Fig. 6, could be determined by Eq. (3) as shown in Fig. 12b. The peak shock pressure decreased during its propagation from 0.1 to 2.0 mm. It is to be noted that the water exhibits the lowest pressure mainly due to the impedance mismatch between the water and the aluminum plate. Actually, the water shows the slowest pressure attenuation behavior. The higher the mass fraction of silica nanoparticles, the faster the decay of the peak shock pressure, indicating the excellent shock attenuation property of the 68 wt% STF and suggesting the promising of the STFs with high mass fractions of nanoparticles as superior protective materials.

The attenuation of shock waves in STF can be primarily attributed to an abrupt viscosity increase under shock. Waitukaitis and Jaeger [30] demonstrated that upon the direct impact of a rod on the STF, an impact-induced jammed solid is formed quickly. As a shock wave propagates in the STF, the initial evenly-dispersed nanoparticles can also form a jammed or densely packed structure, enabling rapid stress attenuation by overcoming the short-range hydrodynamic lubrication forces between nanoparticles [28]. Consequently, the bulk viscosity of the STF experiences a significant increase once the thickening behavior is initiated. The scattering phenomenon resulting from the numerous interfaces between the liquid PEG and solid silica nanoparticles, also contributes to the fast shock wave attenuation in STF. The study by Tian et al. [3] indicated that structures with increased interface density exhibited improved energy absorption capacity. Due to impact-induced jamming and the numerous interfaces of the STF, remarkable energy can be dissipated during the thickening process and the numerous reflections of shock waves between nanoparticles, resulting in the rapid attenuation of shock waves in STF. The higher the mass fraction of nanoparticles in STF, the faster the shock wave attenuation.

4. Conclusions

This paper studies the dynamic response of STFs under laser-induced shock, and the effects of the mass fraction of silica nanoparticles are investigated. The main conclusions are drawn as follows.

(1) The rheology of the PEG, the 40 wt% STF, and the 68 wt% STF are measured, showing that the viscosity increases with increasing the mass fraction of silica nanoparticles. The 68 wt% STF exhibits significant shear-thickening behavior, while the PEG and the 40 wt% STF act as Newtonian fluids in the shear rate range of the experiments.

(2) An effective method combined with laser-induced shock loadings on aluminum-STF-aluminum sandwiched structure and numerical simulations is developed to capture successfully the shock response of STFs under high pressure and ultra-high strain rates.

(3) The first-order and second-order Mie-Grüneisen EOS are established for the first time for the PEG, the 40 wt% STF, and the 68 wt% STF. With increasing the mass fraction of silica nanoparticles, the intercept value (C_0) and the linear slope (S_1) of both the first-order and the second-order EOS increases, while the S_2 of the second-order EOS decreases.

(4) Both the first-order and the second-order EOS could well describe the behavior of the 68 wt% STF at a high particle velocity range, which might be due to the thickening behavior of the STF under high shock pressure. However, the first-order EOS deviates from the second-order EOS at high shock pressure for the PEG and the 40 wt% STF, implying their fluid properties under the present conditions.

(5) The attenuation velocity of the shock wave increases with increasing the mass fraction of silica nanoparticles, indicating the high shock attenuation capacity of the 68 wt%

STF and suggesting the promising of the STFs with high mass fractions of nanoparticles as superior protective materials.

Conflict of interest *On behalf of all authors, the corresponding author states that there is no conflict of interest.*

Author contributions ***Zhoupeng Gu****: Methodology, Investigation, Writing – original draft.* ***Chun Wei****: Methodology, Validation.* ***Xianqian Wu****: Conceptualization, Writing – review & editing, Supervision, Project administration.* ***Chenguang Huang:*** *Writing – review & editing.*

Acknowledgements *This work was supported by the National Key R&D Program of China (Grant No. 2021YFA0719200), the National Natural Science Foundation of China (Grant Nos. 12272391 and 12232020). The authors wish to express their appreciation to Dr. Zhongping Liu at the Institute of Chemical Materials, China Academy of Engineering Physics, for helpful discussion and suggestions on the details of the material preparation.*

1 C. Xiang, Q. Qin, M. Wang, X. Yu, S. Chen, W. Zhang, Y. Xia, J. Zhang, J. Zhao, and T. Wang, Low-velocity impact response of sandwich beams with a metal foam core: Experimental and theoretical investigations, Int. J. Impact Eng. **130**, 172 (2019).
2 C. Pu, X. Yang, H. Zhao, Z. Chen, D. Xiao, C. Zhou, and B. Xue, Numerical study on crack propagation under explosive loads, Acta Mech. Sin. **38**, 421376 (2022).
3 Y. Tian, R. Yang, Z. Gu, H. Zhao, X. Wu, S. T. Dehaghani, H. Chen, X. Liu, T. Xiao, A. McDonald, H. Li, and X. Chen, Ultrahigh cavitation erosion resistant metal-matrix composites with biomimetic hierarchical structure, Compos. Part B-Eng. **234**, 109730 (2022).
4 S. Talebi, M. Sadighi, and M. M. Aghdam, Numerical and experimental analysis of the closed-cell aluminium foam under low velocity impact using computerized tomography technique, Acta Mech. Sin. **35**, 144 (2019).
5 C. Lv, G. Wang, X. Zhang, B. Luo, N. Luo, F. Wu, H. Wu, F. Tan, J. Zhao, C. Liu, and C. Sun, Spalling modes and mechanisms of shocked nanocrystalline NiTi at different loadings and temperatures, Mech. Mater. **161**, 104004 (2021).
6 K. Yang, L. Rao, L. Hu, F. Pan, Q. Yin, and Y. Chen, Flexible, efficient and adaptive modular impact-resistant metamaterials, Int. J. Mech. Sci. **239**, 107893 (2023).
7 K. Jiang, J. Li, B. Gan, T. Ye, L. Chen, and T. Suo, Dynamically compressive behaviors and plastic mechanisms of a CrCoNi medium entropy alloy at various temperatures, Acta Mech. Sin. **38**, 421550 (2022).
8 M. Chen, M. Fu, and L. Hu, Poisson's ratio sign-switching metamaterial with stiffness matrix asymmetry and different elastic moduli under tension and compression, Compos. Struct. **275**, 114442 (2021).
9 X. Li, L. Xiao, and W. Song, Compressive behavior of selective laser melting printed Gyroid structures under dynamic loading, Addit. Manuf. **46**, 102054 (2021).
10 J. Zhang, K. Liu, Y. Ye, and Q. Qin, Low-velocity impact of rectangular multilayer sandwich plates, Thin-Walled Struct. **141**, 308 (2019).
11 Q. Hu, G. Lu, N. Hameed, and K. M. Tse, Dynamic compressive behaviour of shear thickening fluid-filled honeycomb, Int. J. Mech. Sci. **229**, 107493 (2022).
12 F. Gao, Q. Zeng, J. Wang, Z. Liu, and J. Liang, Compressive properties and energy absorption of BCC lattice structures with bio-inspired gradient design, Acta Mech. Sin. **38**, 421345 (2022).
13 G. Lin, J. Li, F. Li, P. Chen, and W. Sun, Low-velocity impact response of sandwich composite panels with shear thickening gel filled honeycomb cores, Compos. Commun. **32**, 101136 (2022).
14 A. Khodadadi, G. Liaghat, S. Vahid, A. R. Sabet, and H. Hadavinia, Ballistic performance of Kevlar fabric impregnated with nanosilica/PEG shear thickening fluid, Compos. Part B-Eng. **162**, 643 (2019).
15 S. Zhang, S. Wang, T. Hu, S. Xuan, H. Jiang, and X. Gong, Study the safeguarding performance of shear thickening gel by the mechanoluminescence method, Compos. Part B-Eng. **180**, 107564 (2020).
16 M. Wei, K. Lin, and L. Sun, Shear thickening fluids and their applications, Mater. Des. **216**, 110570 (2022).
17 X. Fan, Y. Wang, S. Wang, and X. Gong, Suppression of the sutural interface on vibration behaviors of sandwich beam with shear stiffening gel, Compos. Struct. **295**, 115864 (2022).
18 X. Zhang, P. Wang, A. Kurkin, Q. Chen, X. Gong, Z. Zhang, E. H. Yang, and J. Yang, Mechanical response of shear thickening fluid filled composite subjected to different strain rates, Int. J. Mech. Sci. **196**, 106304 (2021).
19 J. Wu, Y. Wang, J. Zhang, C. Zhao, Z. Fan, Q. Shu, X. He, S. Xuan, and X. Gong, A lightweight aramid-based structural composite with ultralow thermal conductivity and high-impact force dissipation, Matter **5**, 2265 (2022).
20 Z. Fan, C. Zhao, J. Wu, Y. Cai, J. Zhou, J. Zhang, X. Gong, and S. Xuan, Intelligent safeguarding Leather with excellent energy absorption via the toughness-flexibility coupling designation, Compos. Part A-Appl. Sci. Manuf. **161**, 107078 (2022).
21 O. E. Petel, and J. D. Hogan, An investigation of shear thickening fluids using ejecta analysis techniques, Int. J. Impact Eng. **93**, 39 (2016).
22 K. Yu, H. Cao, K. Qian, X. Sha, and Y. Chen, Shear-thickening behavior of modified silica nanoparticles in polyethylene glycol, J. Nanopart. Res. **14**, 747 (2012).
23 W. Jiang, X. Gong, S. Xuan, W. Jiang, F. Ye, X. Li, and T. Liu, Stress pulse attenuation in shear thickening fluid, Appl. Phys. Lett. **102**, 101901 (2013).
24 J. Qin, G. Zhang, X. Shi, and M. Tao, Study of a shear thickening fluid: the dispersions of silica nanoparticles in 1-butyl-3-methylimidazolium tetrafluoroborate, J. Nanopart. Res. **17**, 333 (2015).
25 T. Fan, S. S. Xue, W. B. Zhu, Y. Y. Zhang, Y. Q. Li, Z. K. Chen, P. Huang, and S. Y. Fu, Multifunctional polyurethane composite foam with outstanding anti-impact capacity for soft body armors, ACS Appl. Mater. Interfaces **14**, 13778 (2022).
26 J. Q. Zhu, Z. P. Gu, Z. P. Liu, F. C. Zhong, X. Q. Wu, and C. G. Huang, Silicone rubber matrix composites with shear thickening fluid microcapsules realizing intelligent adaptation to impact loadings, Compos. Part B-Eng. **247**, 110312 (2022).
27 R. L. Hoffman, Explanations for the cause of shear thickening in concentrated colloidal suspensions, J. Rheol. **42**, 111 (1998).
28 X. Cheng, J. H. McCoy, J. N. Israelachvili, and I. Cohen, Imaging the microscopic structure of shear thinning and thickening colloidal suspensions, Science **333**, 1276 (2011).
29 J. Zhang, Y. Wang, H. Deng, J. Zhou, S. Liu, J. Wu, M. Sang, and X. Gong, A high anti-impact STF/Ecoflex composite structure with a sensing capacity for wearable design, Compos. Part B-Eng. **233**, 109656 (2022).
30 S. R. Waitukaitis, and H. M. Jaeger, Impact-activated solidification of dense suspensions via dynamic jamming fronts, Nature **487**, 205 (2012).
31 X. Wu, F. Zhong, Q. Yin, and C. Huang, Dynamic response of shear thickening fluid under laser induced shock, Appl. Phys. Lett. **106**, 071903 (2015).
32 E. Balali, N. Kordani, and A. Sadough Vanini, Response of glass fiber-reinforced hybrid shear thickening fluid (STF) under low-velocity impact, J. Textile Institute **108**, 376 (2017).
33 U. Mawkhlieng, and A. Majumdar, Deconstructing the role of shear thickening fluid in enhancing the impact resistance of high-performance fabrics, Compos. Part B-Eng. **175**, 107167 (2019).
34 I. R. Peters, S. Majumdar, and H. M. Jaeger, Direct observation of dynamic shear jamming in dense suspensions, Nature **532**, 214 (2016).
35 N. C. Crawford, L. B. Popp, K. E. Johns, L. M. Caire, B. N. Peterson, and M. W. Liberatore, Shear thickening of corn starch suspensions:

Does concentration matter? J. Colloid Interface Sci. **396**, 83 (2013).
36 A. Fall, N. Huang, F. Bertrand, G. Ovarlez, and D. Bonn, Shear thickening of cornstarch suspensions as a reentrant jamming transition, Phys. Rev. Lett. **100**, 018301 (2008).
37 A. S. Lim, S. L. Lopatnikov, N. J. Wagner, and J. W. Gillespie Jr., Investigating the transient response of a shear thickening fluid using the split Hopkinson pressure bar technique, Rheol. Acta **49**, 879 (2010).
38 M. Osial, M. Nowicki, E. Klejman, and L. Frąś, Investigation of the well-dispersed magnetorheological oil-based suspension with superparamagnetic nanoparticles using modified split Hopkinson pressure bar, Rheol. Acta **61**, 111 (2022).
39 Z. Tan, H. Ma, H. Zhou, X. Han, and C. Cho, The influence of graphene on the dynamic mechanical behaviour of shear thickening fluids, Adv. Powder Tech. **30**, 2416 (2019).
40 O. E. Petel, S. Ouellet, J. Loiseau, D. L. Frost, and A. J. Higgins, A comparison of the ballistic performance of shear thickening fluids based on particle strength and volume fraction, Int. J. Impact Eng. **85**, 83 (2015).
41 O. E. Petel, S. Ouellet, J. Loiseau, B. J. Marr, D. L. Frost, and A. J. Higgins, The effect of particle strength on the ballistic resistance of shear thickening fluids, Appl. Phys. Lett. **102**, 064103 (2013).
42 O. E. Petel, and S. Ouellet, Dynamic strength, particle deformation, and fracture within fluids with impact-activated microstructures, J. Appl. Phys. **122**, 025108 (2017).
43 S. Gürgen, and T. Yıldız, Stab resistance of smart polymer coated textiles reinforced with particle additives, Compos. Struct. **235**, 111812 (2020).
44 S. Gürgen, An investigation on composite laminates including shear thickening fluid under stab condition, J. Compos. Mater. **53**, 1111 (2019).
45 S. Gürgen, F. A. O. Fernandes, R. J. A. de Sousa, and M. C. Kuşhan, Development of eco-friendly shock-absorbing cork composites enhanced by a non-Newtonian fluid, Appl Compos Mater **28**, 165 (2021).
46 S. Gürgen, M. C. Kuşhan, and W. Li, Shear thickening fluids in protective applications: A review, Prog. Polym. Sci. **75**, 48 (2017).
47 Z. P. Gu, X. Q. Wu, Q. M. Li, Q. Y. Yin, and C. G. Huang, Dynamic compressive behaviour of sandwich panels with lattice truss core filled by shear thickening fluid, Int. J. Impact Eng. **143**, 103616 (2020).
48 X. Wu, K. Xiao, Q. Yin, F. Zhong, and C. Huang, Experimental study on dynamic compressive behaviour of sandwich panel with shear thickening fluid filled pyramidal lattice truss core, Int. J. Mech. Sci. **138-139**, 467 (2018).
49 M. R. Sheikhi, and S. Gürgen, Deceleration behavior of multi-layer cork composites intercalated with a non-Newtonian material, Archiv. Civ. Mech. Eng **23**, 2 (2022).
50 X. Wu, Q. Yin, and C. Huang, Experimental study on pressure, stress state, and temperature-dependent dynamic behavior of shear thickening fluid subjected to laser induced shock, J. Appl. Phys. **118**, 173102 (2015).
51 A. Van Blaaderen, J. Van Geest, and A. Vrij, Monodisperse colloidal silica spheres from tetraalkoxysilanes: Particle formation and growth mechanism, J. Colloid Interface Sci. **154**, 481 (1992).
52 T. Parpaite, B. Otazaghine, A. Taguet, R. Sonnier, A. S. Caro, and J. M. Lopez-Cuesta, Incorporation of modified Stöber silica nanoparticles in polystyrene/polyamide-6 blends: Coalescence inhibition and modification of the thermal degradation via controlled dispersion at the interface, Polymer **55**, 2704 (2014).
53 Z. P. Gu, Y. J. Cheng, K. L. Xiao, K. Li, X. Q. Wu, Q. M. Li, and C. G. Huang, Geometrical scaling law for laser-induced micro-projectile impact testing, Int. J. Mech. Sci. **223**, 107289 (2022).
54 X. Wu, Q. Tan, and C. Huang, Geometrical scaling law for laser shock processing, J. Appl. Phys. **114**, 043105 (2013).
55 X. Wu, C. Huang, X. Wang, and H. Song, A new effective method to estimate the effect of laser shock peening, Int. J. Impact Eng. **38**, 322 (2011).
56 X. Wu, Z. Duan, H. Song, Y. Wei, X. Wang, and C. Huang, Shock pressure induced by glass-confined laser shock peening: Experiments, modeling and simulation, J. Appl. Phys. **110**, 053112 (2011).
57 O. T. Strand, D. R. Goosman, C. Martinez, T. L. Whitworth, and W. W. Kuhlow, Compact system for high-speed velocimetry using heterodyne techniques, Rev. Sci. Instruments **77**, 083108 (2006).
58 X. Wu, X. Wang, Y. Wei, H. Song, and C. Huang, An experimental method to measure dynamic stress-strain relationship of materials at high strain rates, Int. J. Impact Eng. **69**, 149 (2014).
59 P. L. N. Fernando, D. Mohotti, and A. Remennikov, Behaviour of explosively welded impedance-graded multi-metal composite plates under near-field blast loads, Int. J. Mech. Sci. **163**, 105124 (2019).
60 W. R. Tang, Z. W. Zhu, T. T. Fu, Z. W. Zhou, and Z. H. Shangguan, Dynamic experiment and numerical simulation of frozen soil under confining pressure, Acta Mech. Sin. **36**, 1302 (2020).
61 D. Fang, W. Li, T. Cheng, Z. Qu, Y. Chen, R. Wang, and S. Ai, Review on mechanics of ultra-high-temperature materials, Acta Mech. Sin. **37**, 1347 (2021).
62 R. Panciroli, S. Abrate, G. Minak, and A. Zucchelli, Hydroelasticity in water-entry problems: Comparison between experimental and SPH results, Compos. Struct. **94**, 532 (2012).
63 K. Bao, X. Zhang, G. Wang, T. Chong, J. Deng, D. Han, and M. Tan, Refractive index of $MgAl_2O_4$ transparent ceramic under quasi-isentropic compression loading, High Pressure Res. **41**, 209 (2021).
64 L. Vočadlo, J. P. Poirer, and G. D. Price, Grüneisen parameters and isothermal equations of state, Am. Miner. **85**, 390 (2000).
65 X. Yang, X. Zeng, H. Chen, Y. Wang, L. He, and F. Wang, Molecular dynamics investigation on complete Mie-Grüneisen equation of state: Al and Pb as prototypes, J. Alloys Compd. **808**, 151702 (2019).
66 O. E. Petel, and A. J. Higgins, Shock wave propagation in dense particle suspensions, J. Appl. Phys. **108**, 114918 (2010).

强激光诱导冲击波加载下剪切增稠流体的动力学行为

谷周澎, 魏春, 吴先前, 黄晨光

摘要 剪切增稠流体(STF)的冲击响应行为是其相关防护工程设计的基础. 本文研究了STF在强激光诱导冲击加载下的动力学行为, 分析了纳米颗粒质量分数的影响规律. 首先制备了不同质量分数的二氧化硅-聚乙二醇(PEG)STF. 采用PDV系统分别测量了不同厚度水、PEG、40%质量分数STF(40 wt% STF)以及68%质量分数STF(68 wt% STF)在强激光诱导冲击加载下的动态响应规律, 并由此得到了材料的状态方程. 结果表明, 材料中的冲击波速度随二氧化硅质量分数的增加而增加, 证明了68 wt% STF优异的冲击能量耗散能力, 为STF在冲击防护工程中的应用提供了关键科学支撑.